Nano Research

Open Access

Research Article

Continuous modulation of oxygen vacancies in MoO_{3-x} quantum dots enables to tunable nitrogen reduction reactivity

Zhihao Lu[1], Yingying Wei[2], Teng Wang[1], Renquan Hu[1], Ning Xu[1], Fangjun Cao[3]✉, Jianping Lai[2], and Yong Yang[1]✉

[1] *State Key Laboratory of Solidification Processing, Center of Advanced Lubrication and Seal Materials, Northwestern Polytechnical University, Xi'an 710072, China*
[2] *State Key Laboratory Base of Eco-Chemical Engineering, Ministry of Education, International Science and Technology Cooperation Base of Eco-Chemical Engineering and Green Manufacturing, College of Chemistry and Molecular Engineering, Qingdao University of Science and Technology, Qingdao 266042, China*
[3] *Shaanxi Key Laboratory of Qinling Ecological Security, Shaanxi Key Laboratory for Animal Conservation, Shaanxi Institute of Zoology, Xi'an 710072, China*

Cite this article: *Nano Research*, **2026**, *19*, 94908514. https://doi.org/10.26599/NR.2026.94908514

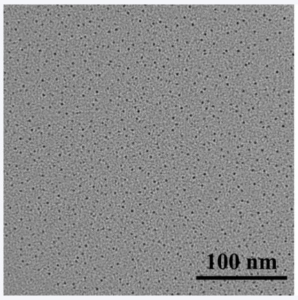

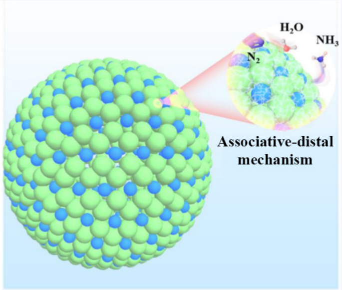

ABSTRACT: The electrochemical nitrogen reduction reaction (eNRR) is a sustainable pathway for ammonia production, yet its practical implementation is hindered by the inherent thermodynamic stability of nitrogen and the competitive hydrogen evolution reaction (HER). Therefore, designing efficient electrocatalysts with superior eNRR activity and selectivity remains challenging. In this work, ultrasmall molybdenum oxide quantum dots (MoO_{3-x} QDs) rich in oxygen vacancies (OVs) were synthesized through an ultrafast wet-chemical approach. Owing to the exceptionally high surface-to-volume ratio, the 3 nm quantum-confined architecture of the MoO_{3-x} QDs has a high density of accessible active sites, facilitating charge transfer kinetics at the nanoscale. The number of OVs within MoO_{3-x} QDs can be precisely tailored by adjusting the amount of ligand introduced and effectively modifying the electronic structure of neighboring Mo sites in favor of the adsorption and hydrogenation of nitrogen, enhancing eNRR selectivity. Owing to the synergistic effects of quantum confinement and vacany engineering, the optimized MoO_{3-x} QD catalysts exhibit outstanding eNRR performance, achieving a good NH_3 yield rate of 38.55 $\mu g \cdot h^{-1} \cdot mg^{-1}$ with a Faradaic efficiency of 8.2% at −0.15 V (vs. RHE), which surpasses that of most reported Mo-based eNRR catalysts under comparable conditions. Furthermore, *in situ* Fourier transform infrared (FTIR) characterization revealed that the eNRR reaction pathway of MoO_{3-x} QDs follows an associative distal mechanism. This work establishes a dual-modulation strategy that integrates quantum size effects with vacancy engineering, providing a promising avenue for designing transition metal oxide catalysts with enhanced activity and selectivity in multielectron transfer reactions.

KEYWORDS: nitrogen reduction reaction, quantum dots, oxygen vacancy, molybdenum oxide

1 Introduction

Ammonia, a cornerstone chemical feedstock for global agriculture and industrial processes, faces an exponentially growing demand in emerging energy applications such as hydrogen carriers and carbon-free fuels. While the century-old Haber–Bosch process currently dominates ammonia synthesis, its reliance on fossil fuel-derived hydrogen and extreme operating conditions (350–500 °C, 150–300 atm) contributes to 1.8% of global CO_2 emissions [1–3]. The electrochemical nitrogen reduction reaction (eNRR) has emerged as a sustainable alternative, enabling decentralized ammonia production under ambient conditions via renewable electricity [4–6]. However, the kinetically inert N≡N triple bond (941 $kJ \cdot mol^{-1}$ dissociation energy) and parasitic hydrogen evolution reaction pose fundamental challenges, demanding catalysts that simultaneously achieve efficient N_2 activation, selective proton-coupled electron transfer, and hydrogen evolution reaction (HER) suppression.

Inspired by the Mo based cofactor in nitrogenase enzymes, molybdenum-based materials have garnered significant attention

Received: January 4, 2026; **Revised:** January 30, 2026
Accepted: January 30, 2026

✉Address correspondence to Fangjun Cao, Fang198789@xab.ac.cn; Yong Yang, yongyangfj@nwpu.edu.cn

for their intrinsic N_2-binding capability and tunable electronic structures [7, 8]. Recent advances in MoS_2 nanosheets [9–11], MoO_2 nanoparticles [12, 13], and Mo_2C heterostructures [14, 15] have demonstrated moderate eNRR activities. Mo_2C-MoO_2 heterostructure quantum dots embedded in reduced graphene oxide (RGO) were proposed as efficient catalysts for the eNRR by Lv and his team [16]. The ultrasmall size of the quantum dot is beneficial for exposing the active sites for the eNRR, and the synergetic effect of Mo_2C and MoO_2 can promote N_2 adsorption and activation and suppress the competitive HER simultaneously. And a self-sacrificial strategy using g-C_3N_4 as templates is proposed by Liu to synthesize 1T-MoS_2 with an ultrahigh 1T content (75.44%), which yields excellent eNRR performances with an ammonia formation rate of 71.07 $\mu g \cdot h^{-1} \cdot mg_{cat}^{-1}$ at –0.5 V versus RHE and a Faradic efficiency of 21.01% [17]. But these systems remain three critical limitations: (1) insufficient exposure of Mo-centered active sites due to bulk-phase aggregation, (2) unfavorable N_2 adsorption/activation dynamics at defect-free surfaces, and (3) structural degradation during prolonged operation. These bottlenecks underscore the need for innovative catalyst architectures that integrate atomic-scale site engineering with operational stability.

Recently, advanced catalyst design strategies focusing on interface engineering, defect modulation, and single-atom incorporation have shown great promise in enhancing catalytic performance across various electrochemical reactions. For instance, the construction of heterostructures has been proven to optimize intermediate adsorption and accelerate charge transfer kinetics via strong interfacial interactions [18]. Similarly, the introduction of oxygen vacancies and anchoring of single atoms can effectively regulate electronic structures and create high-density active sites, thereby improving both activity and stability [19, 20]. Furthermore, innovative synthesis methods, such as colloidal atomic layer deposition and radiation-induced *in situ* reduction, enable precise control over catalyst structures at the nanoscale, offering new avenues for fabricating high-performance hybrid materials [21].

In addition, relevant researchers have noticed that the rational construction of oxygen vacancies in catalysts can effectively enhance their electrocatalytic activity [22, 23]. Studies on MoO_2 with confined surface oxygen vacancies demonstrated that the vacancies enable electron transfer from defective Mo sites to N_2 molecules. This electron donation promotes chemical adsorption of N_2, which is a prerequisite for its subsequent activation [24]. Research on MoO_{3-x}/MXene showed that while oxygen vacancies (OVs) effectively adsorb and activate N_2, they may bind intermediates too strongly, hindering NH_3 desorption [25]. The synergy between OVs and the MXene heterostructure helps fine-tune the electron density around the OVs, weakening the adsorption of intermediates and facilitating NH_3 release. And OVs create localized sites that have a higher affinity for N_2 than for H^+ ions. Research of MoO_{3-x}/MXene also demonstrates that OVs on MoO_{3-x} serve as the active sites for N_2 chemisorption and activation, while the MXene substrate can further regulate the oxygen vacancy sites to break the scaling relation to effectively stabilize $^*N_2/^*N_2H$ while destabilizing $^*NH_2/^*NH_3$, resulting in more optimized binding affinity of eNRR intermediates toward reduced energy barriers and an enhanced eNRR activity for MoO_{3-x}/MXene [25].

Herein, we present a dual engineering strategy that combines quantum confinement and defect modulation to construct sulfur-anchored, oxygen-deficient molybdenum oxide quantum dots (MoO_{3-x} QDs) for high-efficiency eNRR. Three key innovations distinguish this work: First, 3 nm quantum dots create an ultrahigh density of accessible Mo sites (theoretical surface/volume ratio > 800 $m^2 \cdot g^{-1}$) while enabling rapid interfacial charge transfer via shortened carrier diffusion paths. Second, precisely controlled oxygen vacancies generated through competitive ligand coordination (carboxyl vs. sulfhydryl groups) induce localized electron enrichment at Mo centers, which strengthens d-orbital hybridization with N_2 antibonding orbitals, as confirmed by *in situ* spectroscopic analysis. Third, thiomalate-derived sulfur dopants serve dual functions, they kinetically stabilize quantum dot dispersion through steric/electrostatic effects (< 10% size variation after 50 cycles) and synergistically optimize the hydrogenation energetics of eNRR intermediates. As expected， the optimized catalyst achieves an exceptional NH_3 yield of 38.55 $\mu g \cdot h^{-1} \cdot mg^{-1}$ with a Faradaic efficiency of 8.2% at –0.15 V vs. RHE.

2 Experimental section

2.1 Chemicals

Mercaptosuccinic acid (98%) was obtained from Aladdin Co., Ltd. HCl solution (37%) was obtained from Sinopharm Chemical Reagent Co. Ltd. Ammonium molybdate was obtained from Aladdin Co., Ltd. Sodium molybdate was obtained from Aladdin Co., Ltd. Potassium hydroxide (95%) was obtained from Aladdin Co., Ltd. Lithium sulfate monohydrate was obtained from Maclin Co., Ltd. Nitrogen was purchased from Xi'an Jiahe Co., Ltd.

2.2 Synthesis of MoO_{3-x} QDs

Quantum dots were synthesized according to the Ref. [26]. First, 500 mg ammonium molybdate was dissolved in 20 mL deionized water to obtain an ammonium molybdate solution. A certain amount of mercaptosuccinic acid (25, 50, 100, 200, or 300 mg) as a ligand was dissolved in another 20 mL of deionized water as the mercaptosuccinic acid solution. Then, 2.4 mL of 1 M hydrochloric acid or mercaptosuccinic acid solution was rapidly injected into the ammonium molybdate solution and vigorously stirred for approximately 1 min. After dialyzing the solution, freeze-drying was performed to obtain quantum dot powder.

2.3 Characterization of the materials

Transmission electron microscopy (TEM, FEI Tecnai F20) was used to investigate the micromorphology and internal microstructure of the samples. Atomic force microscopy (AFM, Bruker Dimension ICON) was used to test the size and distribution of the samples. A Bruker BSF0209 diffractometer was used to explore the crystal phases and structures of the samples (40 kV, 40 mA Cu Kα radiation). The surface chemical states were studied through X-ray photoelectron spectroscopy (XPS, Thermo Kalpha). A micro-Raman spectroscope (LabRAM HR Evolution, HORIBA Jobin Yvon) was used to obtain the Raman spectra. An electron paramagnetic resonance spectrometer (EPR, Bruker A300) was used to test for unpaired electrons in the samples to characterize the presence of oxygen vacancies. The X-ray absorption spectra of the Mo K-edge structure were collected, and the data collection was carried out in transmission mode using an ionization chamber for Mo foil and in fluorescence excitation mode using a Lytle detector for the sample. All the spectra were collected under ambient conditions. *In situ*-infrared spectroscopy was used to explore the nitrogen reduction process, and a gold film (approximately 20 nm thick) was first deposited on an ATR crystal (a silicon crystal in this experiment). The gold film served as the working electrode. Approximately 50 microliters of the sample mixture (preparation method described below) were drop-cast onto a gold film and allowed to air dry. The cell was then assembled, and the electrolyte was introduced. The electrode was immersed in the electrolyte, and infrared spectra were collected during the application of the test potential. The entire experimental process was carried out under continuous gas purging.

3 Results and discussion

A schematic representation of the synthesis process for the MoO_{3-x} QDs is shown in Fig. 1(a). Typically, ammonium molybdate is utilized as a reaction precursor to generate molybdic acid by adjusting the pH with hydrochloric acid. This process is then followed by spontaneous dehydration to form molybdenum oxide nuclei. Subsequently, thiomalic acid is added. Due to the rapid reaction kinetics, nucleation occurs extensively while growth time remains short, leading to the formation of quantum dots. Concurrently, ligands quickly coordinate with the newly formed QDs, which effectively suppresses further particle growth and ultimately yields stable quantum dots. The reduction conditions provided by the sulfhydryl groups and the coordination of the carboxyl groups with the MoO_{3-x} QDs lead to the formation of OVs. During the subsequent dialysis process, impurities such as ammonium ions will be removed, which will not affect the subsequent electrochemical process.

As demonstrated in Fig. 1(b), the TEM image of the MoO_{3-x} QDs illustrates their size homogeneity. The AFM image reveals that the object is approximately 3 nanometers in size, which is consistent with the TEM results (Fig. S1 in the Electronic Supplementary Material (ESM)). The high-resolution transmission electron microscopy (HRTEM) image shows that the lattice spacing of the quantum dots is approximately 1.056 Å, corresponding to the (110) crystalline surfaces of molybdenum trioxide (illustration in Fig. 1(b)). In addition, TEM of different ligands (Fig. S2 in the ESM) demonstrate that the same quantum dot structure can be produced by using different amounts of ligands during synthesis. Interestingly, the successful synthesis of similar structures using sodium molybdate as the molybdenum source demonstrates that the reaction process primarily involves molybdate anions reacting with ligands (Fig. S3 in the ESM). To explore the chemical composition of the quantum dots, Fourier transform infrared spectroscopy tests were performed in conjunction with Raman spectroscopy. The infrared spectra of ammonium molybdate, thiomalate, and MoO_{3-x} QDs are shown in Fig. S4 in the ESM. The characteristic peak of the sulfhydryl group (–SH) was present between 2500 and 2600 cm^{-1} in the thiomalate, whereas the peak of the S–S bond was found at 560 cm^{-1} in the quantum dots. This

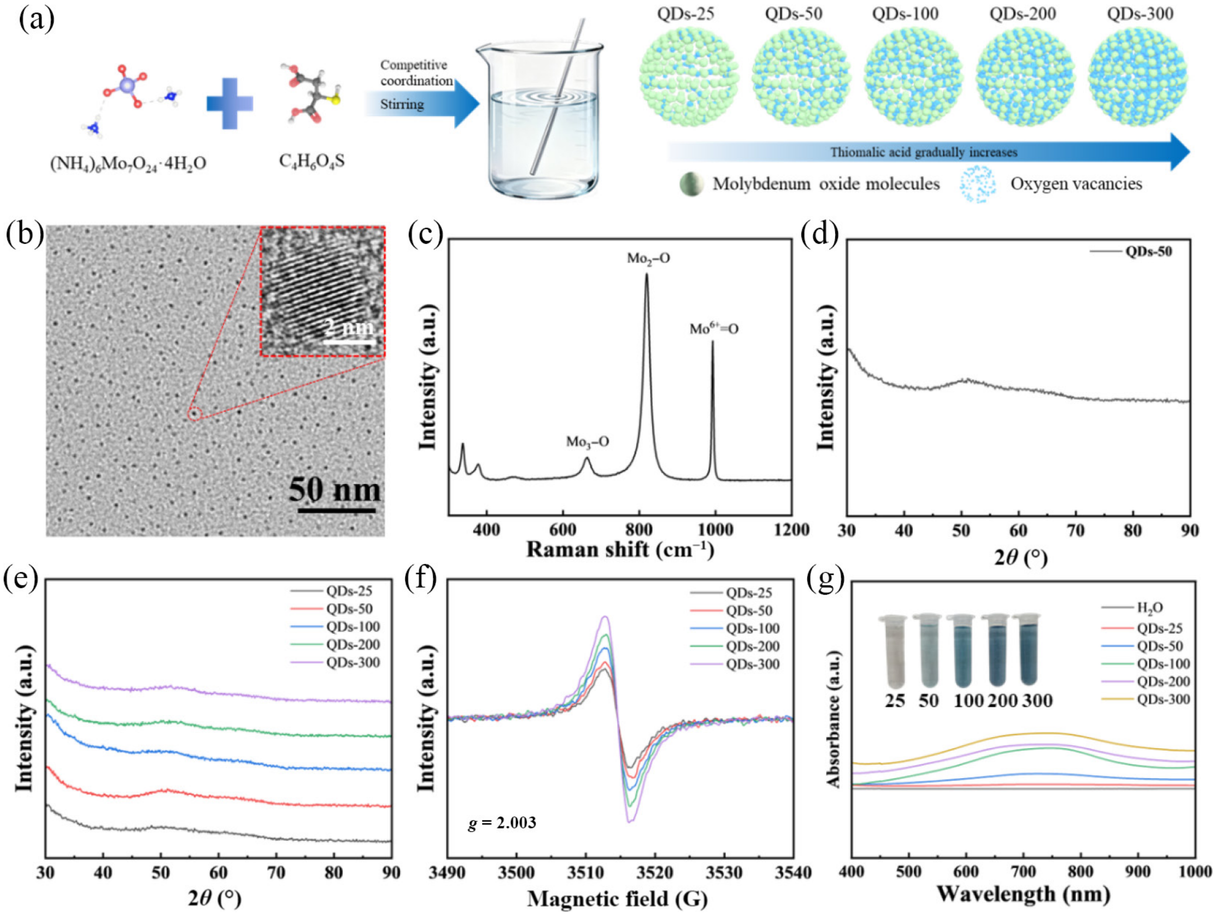

Figure 1 (a) Schematic diagram of quantum dot synthesis. (b) TEM image of MoO_{3-x} QDs-50 (illustration for HRTEM). (c) Raman spectrum of MoO_{3-x} QDs-50. (d) XRD pattern of MoO_{3-x} QDs-50. (e) XRD patterns of MoO_{3-x} QDs-*X* (*X* = 25, 50, 100, 200, 300). (f) EPR spectra of MoO_{3-x} QDs-*X* (*X* = 25, 50, 100, 200, 300). (g) UV absorption spectra of MoO_{3-x} QDs-*X* (*X* = 25, 50, 100, 200, 300).

suggests that a switch between sulfhydryl and disulfide bonding occurs. The strong peak of the quantum dots at 1400 cm^{-1} is indicative of the generation of Mo–S bonds. This finding suggests that the primary component of the synthesized quantum dots is sulfur-doped molybdenum oxide. Furthermore, analysis of the Raman spectrum revealed four prominent peaks at 281, 665, 819, and 991 cm^{-1}, which correspond to the α-MoO$_{3-x}$ phase (Fig. 1(c)) [27, 28]. The occurrence of a double peak at approximately 400 cm^{-1} was observed, which is indicative of a Mo–S bond. Importantly, the X-ray diffraction (XRD) diffraction pattern of the quantum dot sample does not show corresponding signal peaks (Fig. 1(d)). This is primarily attributable to the small size effect of the quantum dots, whose XRD patterns are consistent with those of previous reports [29, 30]. Similarly, quantum dots using different proportions of ligands during the synthesis process exhibit consistent XRD patterns (Fig. 1(e)). The aforementioned tests indicate the successful synthesis of quantum dots. To further explore the composition of the MoO$_{3-x}$ QDs, electronic spin resonance spectroscopy was employed to assess the unpaired electrons of the QD samples. As demonstrated in Fig. 1(f), the g value of the MoO$_{3-x}$ QDs appears to be approximately 2.003, which is a typical signal peak for oxygen vacancies, thereby indicating the presence of a significant number of oxygen vacancies within the sample [31–33]. As the ligand content increases, there is a concomitant increase in the number of oxygen vacancies inside the MoO$_{3-x}$ QDs. With the increase of oxygen vacancies, the color of the solution gradually changes from yellow to blue, and its absorption at 400–1000 nm increases significantly. Rational construction of oxygen vacancies in catalysts can effectively enhance their electrocatalytic activity.

XPS was used to test the chemical state of the Mo and O in the samples. As demonstrated in Figs. 2(a)–2(e), the 3d electron orbital binding energies of molybdenum gradually negatively shifted from 232.71 and 235.87 to 230.49 and 233.72 eV as the mass of the ligand increased (from 25 to 300 mg). This finding suggests a decrease in the mean number of coordination sites with oxygen, thereby demonstrating that the number of oxygen vacancies increases with increasing ligand contents. As the Mo–O coordination number decreases, the valence state of molybdenum element changes from +6 valence to sub oxygen state. On the one hand, the missing oxygen atoms in the lattice can provide more active sites in the catalytic process. On the other hand, excessive oxygen defects will have a negative impact on the stability of the material. And it has been proven that oxygen vacancies can simultaneously adsorb active hydrogen ions and nitrogen gas. Excessive oxygen vacancies will be detrimental to the selective generation of catalytic products.

This phenomenon is further corroborated by the XPS mapping of oxygen (Figs. 2(f)–2(j)). Specifically, with the gradual elevation of ligand dosage, the relative proportion of lattice oxygen decreases progressively, while the concentration of oxygen vacancies exhibits a concomitant increase. When the ligand content reaches 200 mg, the augmented density of oxygen vacancies on the sample surface facilitates the formation of a higher quantity of adsorbed oxygen species. In parallel, the high-resolution XPS spectra of the oxygen element reveal a distinct negative shift in the binding energy of oxygen, a trend that aligns well with the outcomes documented in relevant prior studies. Notably, this observation is also in good agreement with the results derived from EPR spectroscopy analysis. To further consolidate these findings, the local coordination environments of the constituent elements within the samples were subsequently probed via the X-ray absorption near-edge structure (XANES) spectroscopy. Furthermore, the coordination information within the samples was analyzed by X-ray absorption of the near-edge structure to further corroborate our findings.

As shown in Figs. 3(a)–3(c), the Mo K-edge XANES data of the MoO$_{3-x}$ QDs were analyzed with Mo foil, MoO$_3$, and MoS$_2$ as references. Compared to MoO$_3$ (Fig. 3(a)), the XANES spectrum of MoO$_{3-x}$ quantum dots shows significant broadening in both the pre-edge and white-line peaks, indicating a more disordered structure [34]. The Fourier transform (FT) of the extended EXAFS data reveals that the coordination in MoO$_{3-x}$ quantum dots is different from that in MoO$_3$ and MoS$_2$, reflecting the crystal structure of

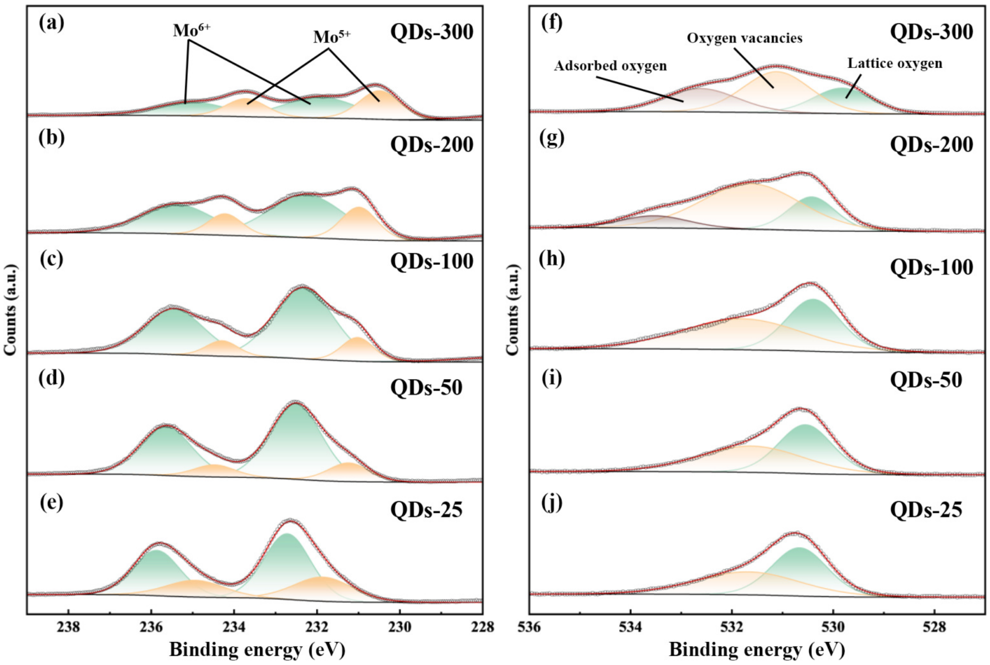

Figure 2 XPS spectra of MoO$_{3-x}$ QDs-X (X = 25, 50, 100, 200, 300): (a)–(e) Mo 3d; (f)–(j) O 1s.

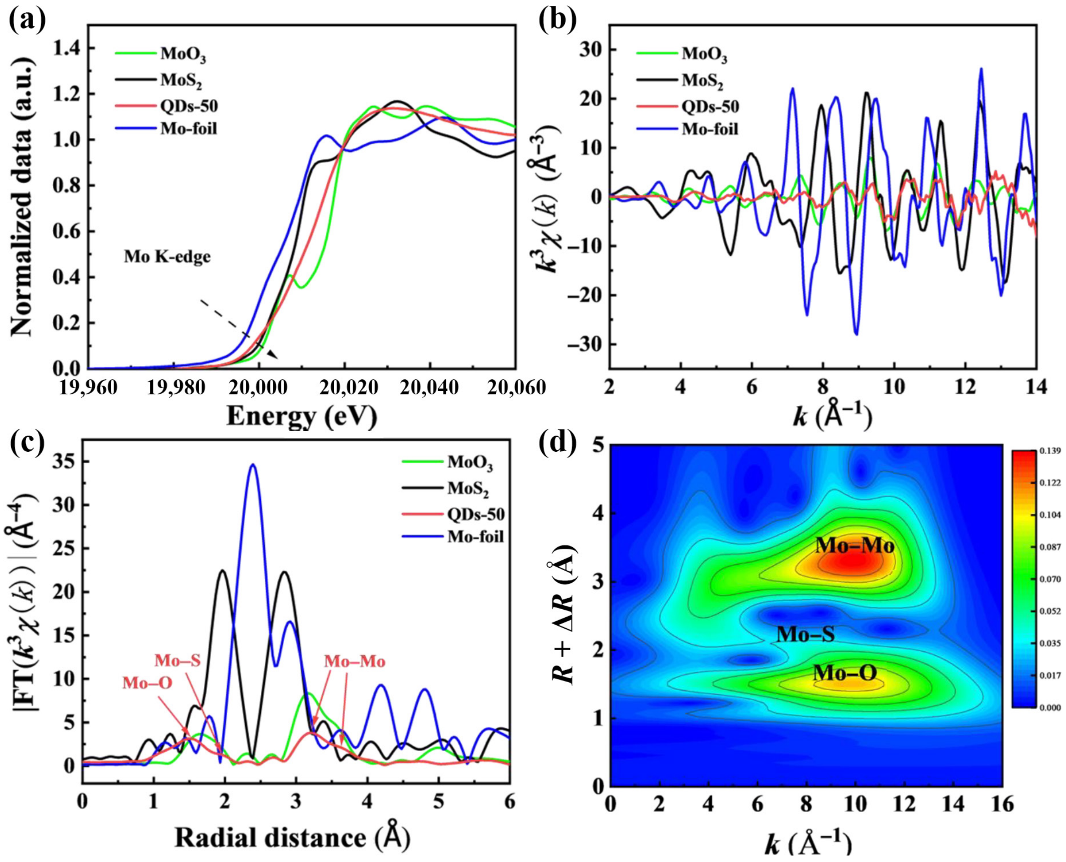

Figure 3 (a) Mo K-edge XANES spectra of MoO$_3$, MoS$_2$, MoO$_{3-x}$ QDs, and Mo-foil. (b) EXAFS spectra of MoO$_3$, MoS$_2$, MoO$_{3-x}$ QDs, and Mo-foil. (c) FT-EXAFS spectra of MoO$_{3-x}$ QDs-50. (d) Chemical stateandlocal coordination environment of MoO$_{3-x}$ QDs-50.

MoO$_{3-x}$ quantum dots (Fig. 3(c)), with one type of Mo–O bond, two types of Mo–Mo bonds, and one type of Mo–S bond. The Mo K-edge XANES spectrum of the Mo$_{3-x}$ QDs implied that the fitted average oxidation state of the Mo species was approximately 1–1.5, which is in good agreement with the XPS results. As shown in Fig. 3(c), the FT EXAFS curve of the MoO$_{3-x}$ QDs shows that the quantum dots exhibit a Mo–O bond at R = 1.503 Å, a Mo–S bond at R = 1.963 Å, and Mo–Mo bonds at R = 3.221 Å and R = 3.620 Å. Detailed structural parameters are summarized in Table S1 in the ESM. Owing to its high accuracy in both the k and R spaces, the wavelet transform (WT, Fig. 3(d)) is considered an appropriate supplement for the FT. WT-EXAFS was subsequently carried out to determine the local structure of Mo in the Mo$_{3-x}$ QDs. An intensity maximum at 10 Å^{-1} assigned to Mo–Mo/O coordination was displayed, while the signal of Mo–S scattering was absent compared with that of MoS$_2$. This further evidences that S atoms are present in quantum dots only in doped form [35–37]. The above characterizations demonstrate the successful synthesis of sulfur atom-doped molybdenum oxide quantum dots.

The eNRR performance of the as-prepared MoO$_{3-x}$ QDs was evaluated at room temperature via an H-type electrolytic cell with an Ar- or N$_2$-saturated 0.1 M KOH electrolyte. First, the linear sweep voltammetry (LSV) curves of MoO$_{3-x}$ QDs-X (X = 25, 50, 100, 200, and 300) show that the current density of MoO$_{3-x}$ QDs-50 is greater than that of the other materials in N$_2$-saturated electrolytes, which indicate that MoO$_{3-x}$ QDs-50 with appropriate oxygen vacancies has optimal eNRR activity (Fig. 4(a)). Moreover, the current density of MoO$_{3-x}$ QDs-50 clearly increases when N$_2$-saturated electrolyte is used instead of Ar-saturated electrolyte, confirming the occurrence of N$_2$ electroreduction to NH$_3$ (Fig. 4(b)). To assess the specific NH$_3$ yield and Faraday efficiency (FE), 1 h chronoamperometry measurements were carried out on catalysts in the range of −0.05 to −0.25 V (vs. RHE) of MoO$_{3-x}$ QDs-50 (Fig. S5 in the ESM). The indophenol-blue method was employed to quantify the NH$_4^+$ or N$_2$H$_4$ concentration in different electrolytes (0.1 M KOH, 0.1 M Li$_2$SO$_4$, and 0.1 M HCl), and the corresponding standard curves are shown in Figs. S6–S9 in the ESM. During the chronoamperometry measurements, MoO$_{3-x}$ QDs-50 showed stable electrocatalytic performance for the eNRR at all potentials. At different potentials (Fig. 4(c)), the NH$_3$ yield and FE of MoO$_{3-x}$ QDs-50 exhibited an optimal NH$_3$ yield rate of 39.55 μg·h^{-1} and an FE of 8.2% at −0.15 V (vs. RHE). As the electrolysis time is extended, the NH$_3$ yield shows a linear increase at −0.15 V vs. RHE (Fig. S10 in the ESM). Ultraviolet–visible (UV–Vis) absorption spectra and corresponding NH$_3$ yields under different conditions demonstrate the origin of NH$_3$ (Fig. S11 in the ESM). As shown in Figs. S12(a) and S12(b) in the ESM, almost no NH$_3$ is detected in the Ar-saturated electrolyte at −0.15 V (vs. RHE) or in the N$_2$-saturated electrolyte at the open-circuit potential (OCP). When only carbon paper (CP) without MoO$_{3-x}$ QDs-50 was used for eNRR, the same sign as the above condition was found, demonstrating that the conductive substrate hardly has eNRR activity. By alternating N$_2$ and Ar bubbling cycles, NH$_3$ production only occurs when N$_2$ is fed into the electrolytic cell, further indicating that ammonia is collected by N$_2$ reduction (Fig. 4(d)). Moreover, no N$_2$H$_4$ production was detected after electrolysis, revealing the excellent selectivity of MoO$_{3-x}$ QDs-50 for the conversion of N$_2$ to NH$_3$ (Fig. S13 in the ESM). Furthermore,

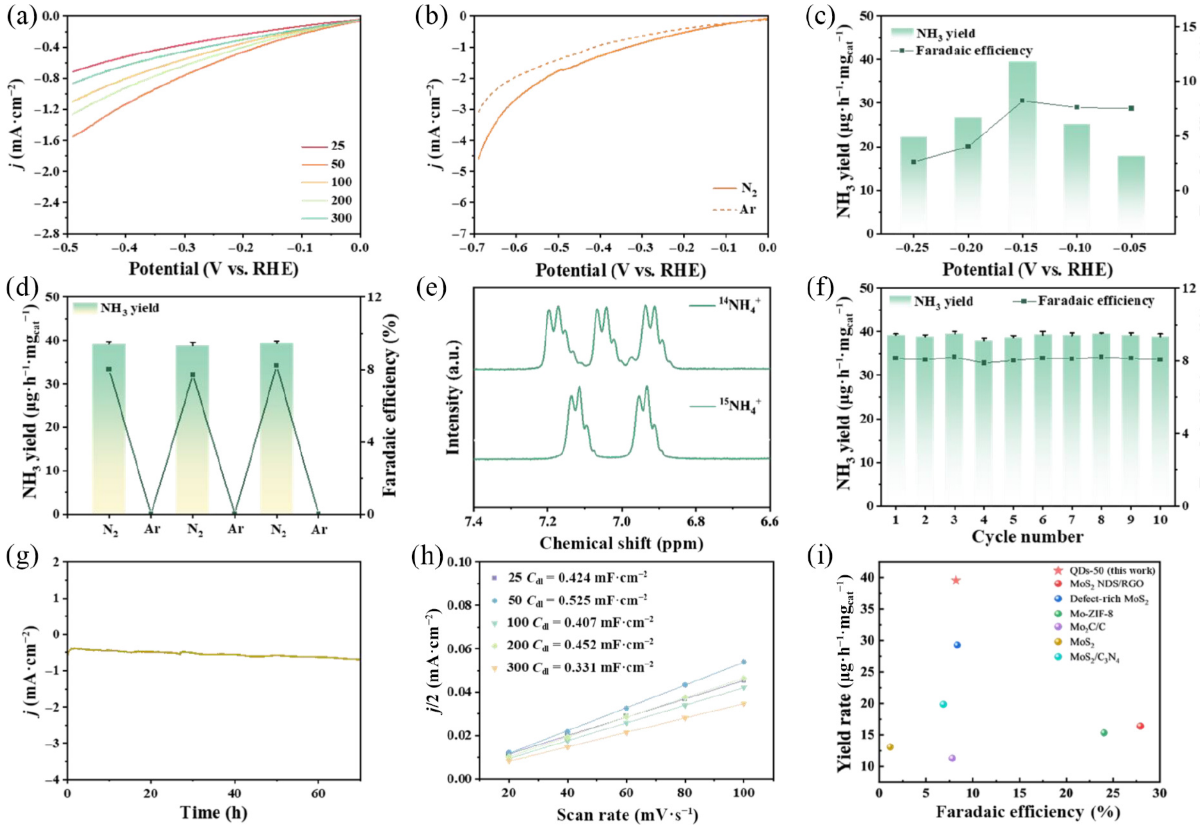

Figure 4 (a) LSV curves of MoO_{3-x} QDs-*X* (25, 50, 100, 200, and 300) in N_2-saturated 0.1 M KOH. (b) LSV curves of MoO_{3-x} QDs-50 acquired in Ar and N_2-saturated 0.1 M KOH. (c) The obtained NH_3 yield and corresponding FEs of MoO_{3-x} QDs-50 at the given potential in N_2-saturated 0.1 M KOH. (d) NH_3 yields and FEs of MoO_{3-x} QDs-50 at a potential of −0.15 V vs. RHE with 3 alternating 1 h cycles between N_2-saturated and Ar-saturated electrolytes for a total of 6 cycles. (e) ^1H-NMR spectra of the electrolyte after electrolysis under $^{15}N_2$-saturated conditions and $^{14}N_2$-saturated conditions. (f) Recycling test for 10 MoO_{3-x} QDs-50 at −0.15 V vs. RHE. (g) Time-dependent current density curve for catalyst-50 at a potential of −0.15 V (vs. RHE) and the NH_3 yield and FE before and after 70 h. (h) C_{dl} extracted from the CV curves. (i) Comparison of the eNRR performance of Mo-based catalysts in H-type cells.

^1H nuclear magnetic resonance (NMR) spectroscopy was used to understand the source of N in NH_3 after electrocatalysis. At −0.15 V (vs. RHE), a double formant from $^{15}NH_4^+$ is observed when $^{15}N_2$ is fed into the reaction cell, but a triple formant from $^{14}NH_4^+$ is not found, indicating that the detected NH_3 is produced by eNRR of MoO_{3-x} QDs-50 (Fig. 4(e)).

To investigate the stability of MoO_{3-x} QDs-50, cycling chronoamperometry tests (Fig. S14 in the ESM) and time-dependent electrolysis tests were conducted. As shown in Fig. 4(f), there are negligible changes in the NH_3 yield and FE for MoO_{3-x} QDs-50 after ten cycles of testing, indicating that it has good cycling stability. In addition, the current density of MoO_{3-x} QDs-50 at −0.15 V (vs. RHE) remains stable for 70 h of continuous electrolysis, indicating its long-term stability (Fig. 4(g)). A comparison of the NH_3 yield and FE of MoO_{3-x} QDs-50 after 70 h with those after 1 h of electrolysis revealed little change, which is consistent with the results of the UV–Vis absorption spectra. Double-layer capacitance (C_{dl}) measurements were performed to determine the electrochemically active surface area (ECSA) of the catalysts toward the eNRR. On the basis of the CV curves of MoO_{3-x} QDs-*X* (Fig. 4(h) and Fig. S15 in the ESM), MoO_{3-x} QDs-50 is calculated to have the largest C_{dl} value (0.525 mF·cm⁻²) compared with that of MoO_{3-x} QDs-25 (0.424 mF·cm⁻²), MoO_{3-x} QDs-100 (0.407 mF·cm⁻²), MoO_{3-x} QDs-200 (0.452 mF·cm⁻²), and MoO_{3-x} QDs-300 (0.331 mF·cm⁻²), suggesting that MoO_{3-x} provides more catalytically active sites for eNRR. The increased ECSA of MoO_{3-x} QDs-300 is attributed to the synergistic effect of oxygen vacancies and S doping. We also investigated the effects of the N_2 flow rate on the NH_3 yield and FE of MoO_{3-x} QDs-50. The results indicate that the N_2 flow rate employed in the eNRR tests can maintain the N_2 saturation condition of the electrolyte and that there is no significant increase in the NH_3 yield or FE with increasing N_2 flow rates (Fig. S16 in the ESM). Integrating structural characterization and electrochemical experimental results, as the concentration of OVs increases—evidenced by the enhanced EPR signal and the negative shift in the Mo 3d binding energy from XPS, the electronic structure of the catalyst undergoes significant changes: The valence state of Mo centers gradually decreases from +6, leading to an elevated d-band electron density. This enhances the hybridization between Mo sites and the antibonding orbitals of N_2, thereby promoting the activation of the N≡N bond. Furthermore, the introduction of OVs creates localized electron-rich regions on the MoO_{3-x} surface, which not only optimizes the chemical adsorption strength of N_2 but also regulates the adsorption energy of key intermediates (e.g., *NNH), lowering the reaction barrier and thus improving the eNRR kinetics. However, the oxygen vacancy concentration that is either too high or too low is detrimental to the reaction. The MoO_{3-x} QDs-25 exhibits fewer oxygen vacancies than MoO_{3-x} QDs-50. This leads to a limited number of active sites (confirmed by a lower C_{dl}) and a reduced overall reaction rate. It also results in insufficient electronic modulation, which weakens N_2 adsorption and activation.

Moreover, the lack of oxygen vacancies may inadequately inhibit the competing HER, explaining the sample's poorer electrochemical performance. When OVs are over-abundant (e.g., in MoO_{3-x} QDs-300), the overly electron-rich surface strengthens the adsorption of H^+, aggravates the competing hydrogen evolution reaction, and results in a decline in Faradaic efficiency. This trend is consistent with the ECSA and LSV results: MoO_{3-x} QDs-50 exhibits a moderate OVs concentration and the largest C_{dl} value (0.525 mF·cm^{-2}), achieving an optimal balance between N_2 adsorption/activation and HER suppression while maintaining high accessibility of active sites. Consequently, it delivers the highest NH_3 yield (38.55 μg·h^{-1}·mg^{-1}) and Faradaic efficiency (8.2%). Compared to other molybdenum-based catalysts (Fig. 4(i) and Table S2 in the ESM), it exhibits certain advantages.

In addition, the eNRR performance of MoO_{3-x} QDs-50 was further investigated in 0.1 M Li_2SO_4 and 0.1 M HCl. As depicted in Figs. S17 and S18 in the ESM, MoO_{3-x} QDs-50 achieves an NH_3 yield of 34.03 μg·h^{-1}·mg$_{\mathrm{cat}}^{-1}$ and an FE of 7.5% in 0.1 M Li_2SO_4. In 0.1 M HCl, the NH_3 yield was 6.98 μg·h^{-1}·mg$_{\mathrm{cat}}^{-1}$ and the FE was 1.1%. Among the Mo-based eNRR catalysts, MoO_{3-x} QDs-50 shows satisfactory performance in terms of the NH_3 yield and FE at lower potentials in alkaline electrolytes (Fig. 4(i)). This research demonstrates a synergistic multimechanism for enhancing eNRR activity and selectivity through the construction of ultrasmall MoO_{3-x} QDs with precisely engineered oxygen vacancies. Active oxygen vacancies create localized electron-rich regions on the surface of the MoO_{3-x} QDs, which significantly strengthen the d–π orbital interaction between the Mo sites and N_2 molecules, facilitating the activation and cleavage of the inert N≡N triple bond. Owing to their ultrasmall size, the QD assembly offers an extremely high surface-to-volume ratio and a high density of accessible active sites, promoting interfacial charge transfer and improving the reaction kinetics.

To further investigate the intermediate species and the reaction mechanism of MoO_{3-x} QDs during the eNRR, the electrochemical *in situ* FTIR tests were conducted. As shown in Fig. 5(c), the absorption peak at 1650 cm^{-1} could be attributed to chemisorbed N_2, suggesting that the MoO_{3-x} QDs exhibit good adsorption ability for dissolved N_2. The peaks at 1420 and 1690 cm^{-1} are caused by the asymmetric and symmetric deformation vibrations of NH_4^+, respectively [38]. The presence of NH_4^+ confirms the continuous production of NH_3. Besides, the increasing absorption peaks at 1541–1457, 1330, and 3245 cm^{-1} are attributated to the H–N–H bending, –NH_2 wagging, and the N–H stretching of adsorbed N_2H_y species, respectively [39]. Notably, the peaks of –N–N stretching located at ~ 1060 cm^{-1} are not found and no N_2H_4 was deteted after eNNR process. Based on these results, it can be speculated that the eNRR mechanism of MoO_{3-x} QDs follows associative distal mechanism. The incorporation of sulfur doping, combined with oxygen vacancies, induces electronic optimization, which effectively lowers the energy barrier for the potential-determining step (NNH* formation) and optimizes the adsorption behavior of key intermediates, favoring the nitrogen reduction pathway. Furthermore, this electronic restructuring selectively increases the energy barrier for hydrogen adsorption, resulting in effective HER suppression, thereby significantly enhancing the Faradaic efficiency and ammonia yield of the eNRR process (Fig. 5(b)). The catalyst achieves efficient and highly selective catalysis of the eNRR pathway through the multifaceted synergy of quantum confinement, defect engineering, and electronic structure modulation.

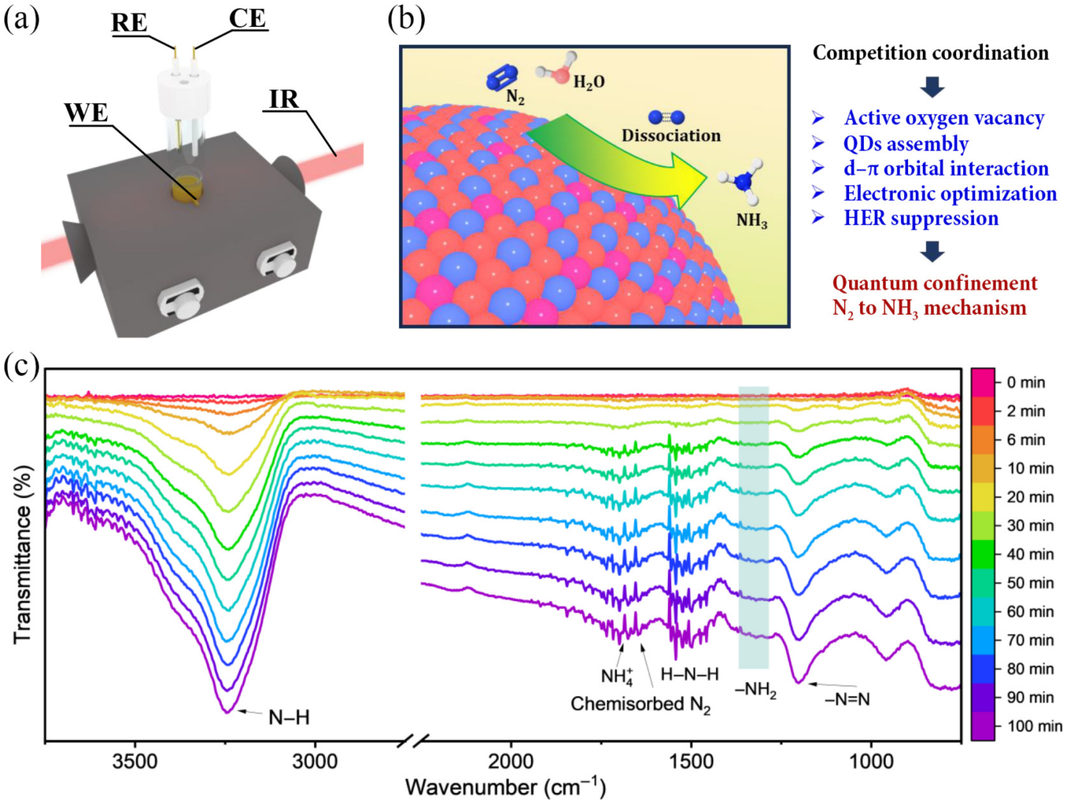

Figure 5 (a) Schematic illustration of the *in situ* infrared testing apparatus. (b) Mechanism diagram of nitrogen reduction using quantum dots. (c) *In situ* infrared spectra obtained from MoO_{3-x} QDs.

4 Conclusion

In this work, we successfully synthesized sulfur-doped molybdenum oxide quantum dots with gradient oxygen vacancies (MoO_{3-x} QDs) through a ligand competition strategy, achieving excellent performance in electrochemical nitrogen reduction. The synergistic effects of quantum confinement (3 nm), controlled oxygen vacancy engineering, and sulfur-mediated dual functionality collectively enhances N_2 activation kinetics while suppressing competitive hydrogen evolution, as evidenced by *in situ* spectroscopic and computational analyses. The optimized catalyst delivers an NH_3 yield of 38.55 $\mu g \cdot h^{-1} \cdot mg^{-1}$ with 8.2% Faradaic efficiency at –0.15 V vs. RHE, alongside exceptional stability. This work establishes a universal paradigm for designing defect-rich quantum materials through atomic-level coordination control, bridging 63% of the energy efficiency gap between electrocatalytic and industrial Haber–Bosch systems. The demonstrated scalability to other transition metal oxides and compatibility with renewable energy inputs position this strategy as a critical step toward decentralized, carbon-neutral ammonia synthesis.

Electronic Supplementary Material: Supplementary material (structural characterization, synchrotron radiation, electrochemical measurements, etc.) is available in the online version of this article at https://doi.org/10.26599/NR.2026.94908514.

Data availability

All data needed to support the conclusions in the paper are presented in the manuscript and the Electronic Supplementary Material. Additional data related to this paper may be requested from the corresponding author upon request.

Acknowledgement

This work was supported by the National Natural Science of China (No. 22171227). We would like to thank the Analytical & Testing Center of Northwestern Polytechnical University for TEM characterizations.

Declaration of competing interest

There are no conflicts to declare.

Author contribution statement

Z. H. L.: Data curation, validation, writing – original draft, experimental design. Y. Y. W., T. W., R. Q. H., and N. X.: Data curation, experimental design. F. J. C. and Y. Y.: Materials synthesis, project administration. J. P. L.: Experimental design. All authors have read and approved the final manuscript.

Use of AI statement

None.

References

[1] Humphreys, J.; Lan, R.; Tao, S. W. Development and recent progress on ammonia synthesis catalysts for haber-bosch process. *Adv. Energy Sustainability Res.* **2021**, *2*, 2000043.

[2] Li, J. Y.; Xiong, Q. C.; Mu, X. W.; Li, L. Recent advances in ammonia synthesis: From haber-bosch process to external field driven strategies. *ChemSusChem* **2024**, *17*, e202301775.

[3] Anastasiadou, D.; Van Beek, Y.; Hensen, E. J. M.; Figueiredo, M. C. Ammonia electrocatalytic synthesis from nitrate. *Electrochem. Sci. Adv.* **2023**, *3*, e2100220.

[4] Zhao, X.; Hu, G. Z.; Chen, G. F.; Zhang, H. B.; Zhang, S. S.; Wang, H. H. Comprehensive understanding of the thriving ambient electrochemical nitrogen reduction reaction. *Adv. Mater.* **2021**, *33*, 2007650.

[5] Chen, C.; Liu, Y.; Yao, Y. Ammonia synthesis via electrochemical nitrogen reduction reaction on iron molybdate under ambient conditions. *Eur. J. Inorg. Chem.* **2020**, *2020*, 3236–3241.

[6] Dong, G.; Huang, C.; Chen, F. Y.; Liu, X. Q.; Li, Z.; Su, X. L.; Zeng, T.; Chen, Y. X.; Chen, Y. H.; Wang, Y. Construction of electron rich Fe active sites by FeCu alloy anchoring on carbon nitride for photocatalytic nitrogen reduction. *Rare Met.* **2024**, *43*, 1570–1579.

[7] Tanifuji, K.; Jasniewski, A. J.; Lee, C. C.; Solomon, J. B.; Nagasawa, T.; Ohki, Y.; Tatsumi, K.; Hedman, B.; Hodgson, K. O.; Hu, Y. L. et al. Incorporation of an asymmetric Mo-Fe-S cluster as an artificial cofactor into nitrogenase. *Chembiochem* **2022**, *23*, e202200384.

[8] Shi, T. Y.; Xie, J. P. Molybdenum enzymes and molybdenum cofactor in mycobacteria. *J. Cell. Biochem.* **2011**, *112*, 2721–2728.

[9] Chen, X. Y.; Lu, S. C.; Wei, Y. J.; Sun, M. J.; Wang, X.; Ma, M.; Tian, J. Basal plane-activated boron-doped MoS_2 nanosheets for efficient electrochemical ammonia synthesis. *ChemSusChem* **2023**, *16*, e202202265.

[10] Zhang, L.; Ji, X. Q.; Ren, X.; Ma, Y. J.; Shi, X. F.; Tian, Z. Q.; Asiri, A. M.; Chen, L.; Tang, B.; Sun, X. P. Electrochemical ammonia synthesis via nitrogen reduction reaction on a MoS_2 catalyst: Theoretical and experimental studies. *Adv. Mater.* **2018**, *30*, 1800191.

[11] Liu, B. P.; Ma, C. Q.; Liu, D.; Yan, S. H. Sulfur-vacancy defective MoS_2 as a promising electrocatalyst for nitrogen reduction reaction under mild conditions. *ChemElectroChem* **2021**, *8*, 3030–3039.

[12] Wang, J. Q.; Jiang, Z.; Peng, G. M.; Hoenig, E.; Yan, G. B.; Wang, M. Z.; Liu, Y. Y.; Du, X. W.; Liu, C. Surface valence state effect of MoO_{2+x} on electrochemical nitrogen reduction. *Adv. Sci.* **2022**, *9*, 2104857.

[13] Muhammed Safeer, N. K.; Sathiskumar, C.; John, N. S. Metallic MoO_2 as a highly selective catalyst for electrochemical nitrogen fixation to ammonia under ambient conditions. *ChemistrySelect* **2023**, *8*, e202203344.

[14] Fan, B. B.; Wang, H. Z.; Zhang, H.; Song, Y.; Zheng, X. R.; Li, C. J.; Tan, Y. Q.; Han, X. P.; Deng, Y. D.; Hu, W. B. Phase transfer of Mo_2C induced by boron doping to boost nitrogen reduction reaction catalytic activity. *Adv. Funct. Mater.* **2022**, *32*, 2110783.

[15] Singh, D.; Tayyebi, E.; Exner, K. S. Statistical approach to the free-energy diagram of the nitrogen reduction reaction on Mo_2C MXene. *ChemElectroChem* **2025**, *12*, e202500196.

[16] Wan, Y. C.; Wang, Z. J.; Li, J.; Lv, R. T. Mo_2C–MoO_2 heterostructure quantum dots for enhanced electrocatalytic nitrogen reduction to ammonia. *ACS Nano* **2022**, *16*, 643–654.

[17] Liu, R. Q.; Guo, T.; Fei, H.; Wu, Z. Z.; Wang, D. Z.; Liu, F. Y. Highly efficient electrocatalytic N_2 reduction to ammonia over metallic 1T phase of MoS_2 enabled by active sites separation mechanism. *Adv. Sci.* **2022**, *9*, 2103583.

[18] Hou, S.; Zhang, A. S.; Zhou, Q.; Wen, Y. J.; Zhang, S. X.; Su, L. F.; Huang, X. J.; Wang, T.; Rui, K.; Wang, C. et al. Designing heterostructured FeP-CoP for oxygen evolution reaction: Interface engineering to enhance electrocatalytic performance. *Nano Res.* **2023**, *16*, 6601–6607.

[19] Yuan, D.; Du, W. Y.; Ma, D. W.; Chu, K. Efficient and sustainable urea synthesis on a bifunctional catalyst. *Nano Res.* **2025**, *18*, 94907910.

[20] Zhang, K.; Mao, X. Z.; Luo, C. W.; Yan, W.; Long, Y. W.; Zhang, M.

J.; Gan, J.; Zeng, H. Y.; Zhang, M. X.; Wu, G. Z. Radiation-induced *in situ* synthesis of Ni anchored MoO_3 with oxygen vacancy for high-performance pseudocapacitor. *Nano Res.* **2026**, *19*, 94907947.

[21] Cao, X. J.; He, P. L. Revealing the effect of hybrid oxide coatings on copper catalysts for CO_2 electroreduction. *Rare Met.* **2025**, *44*, 2861–2864.

[22] Kagdada, H. L.; Jain, A. Impact of vacancy defects on electrochemical nitrogen reduction reaction performance of MXenes. *ChemPhysChem* **2024**, *25*, e202300993.

[23] Li, H. N.; Huang, C. D. Recent advances in the application of structural-phase engineering strategies in electrochemical nitrogen reduction reaction. *Adv. Mater. Interfaces* **2020**, *7*, 2001215.

[24] Zhang, G.; Ji, Q. H.; Zhang, K.; Chen, Y.; Li, Z. H.; Liu, H. J.; Li, J. H.; Qu, J. H. Triggering surface oxygen vacancies on atomic layered molybdenum dioxide for a low energy consumption path toward nitrogen fixation. *Nano Energy* **2019**, *59*, 10–16.

[25] Chu, K.; Luo, Y. J.; Shen, P.; Li, X. C.; Li, Q. Q.; Guo, Y. L. Unveiling the synergy of O-vacancy and heterostructure over MoO_{3-x}/MXene for N_2 electroreduction to NH_3. *Adv. Energy Mater.* **2022**, *12*, 2103022.

[26] Zhong, S. C.; Xing, C. C.; Cao, A.; Zhang, T.; Li, X. J.; Yu, J.; Cai, W. P.; Li, Y. Ultra-fast synthesis of water soluble MoO_{3-x} quantum dots with controlled oxygen vacancies and their near infrared fluorescence sensing to detect H_2O_2. *Nanoscale Horiz.* **2020**, *5*, 1538–1543.

[27] Zou, B.; Wang, X. N.; Zhou, Y.; Zhou, Y.; Wu, Y. Y.; Xing, T. T.; He, Y.; Yang, J. F.; Chen, Y. X.; Ren, P. et al. Optical effect modulation in polarized Raman spectroscopy of transparent layered α-MoO_3. *Small* **2023**, *19*, 2206932.

[28] Sahu, S. R.; Rikka, V. R.; Haridoss, P.; Chatterjee, A.; Gopalan, R.; Prakash, R. A novel α-MoO_3/single-walled carbon nanohorns composite as high-performance anode material for fast-charging lithium-ion battery. *Adv. Energy Mater.* **2020**, *10*, 2001627.

[29] Li, H.; Xu, Q.; Wang, X. Z.; Liu, W. Ultrasensitive surface-enhanced Raman spectroscopy detection based on amorphous molybdenum oxide quantum dots. *Small* **2018**, *14*, 1801523.

[30] Li, H.; Li, Y. Z.; Xu, Q.; Zhang, A. L. Multifunctional clay/PNIPAM hydrogel incorporating H_xMoO_3 plasmonic quantum dot. *Energy Environ. Mater.* **2020**, *3*, 192–201.

[31] Niu, Y. T.; Chen, H. L.; Zhang, Z. X.; Zhang, H. W.; Bai, W. H.; Rong, R.; Cheng, W.; Xie, R. J. Regulation of oxygen vacancies enables ultrastable photoelectrochemical UV photodetection. *Adv. Opt. Mater.* **2025**, *13*, 2500823.

[32] Sun, J.; Wang, C. L.; Bai, C. Z.; Kamran, M.; Zheng, J. H.; Liang, Z. J.; Zhang, R. Q.; Yao, S. D.; Bai, S. T. Oxygen vacancies promoted hydrogenation of MEA-captured-CO_2 to methanol. *ChemCatChem* **2025**, *17*, e00868.

[33] Liu, Y. F.; Ye, C. C.; Chen, L.; Fan, J. B.; Liu, C.; Xue, L.; Sun, J. W.; Zhang, W. Q.; Wang, X.; Xiong, P. et al. High entropy-driven role of oxygen vacancies for water oxidation. *Adv. Funct. Mater.* **2024**, *34*, 2314820.

[34] Yuan, D.; Ma, X.; Su, X. T.; Wang, J. D.; Chen, H. M.; Li, S. Z. MoS_2 nanotubes for boosting electrocatalytic performance of nitrogen to ammonia. *Mater. Lett.* **2023**, *337*, 133787.

[35] Funke, H.; Scheinost, A. C.; Chukalina, M. Wavelet analysis of extended x-ray absorption fine structure data. *Phys. Rev. B* **2005**, *71*, 094110.

[36] Ravel, B.; Newville, M. ATHENA, ARTEMIS, HEPHAESTUS: Data analysis for X-ray absorption spectroscopy using IFEFFIT. *J. Synchrotron Radiat.* **2005**, *12*, 537–541.

[37] Zabinsky, S. I.; Rehr, J. J.; Ankudinov, A.; Albers, R. C.; Eller, M. J. Multiple-scattering calculations of x-ray-absorption spectra. *Phys. Rev. B* **1995**, *52*, 2995–3009.

[38] Song, P. F.; Wang, H.; Kang, L.; Ran, B. C.; Song, H. H.; Wang, R. M. Electrochemical nitrogen reduction to ammonia at ambient conditions on nitrogen and phosphorus co-doped porous carbon. *Chem. Commun.* **2019**, *55*, 687–690.

[39] Ren, J. T.; Wan, C. Y.; Pei, T. Y.; Lv, X. W.; Yuan, Z. Y. Promotion of electrocatalytic nitrogen reduction reaction on N-doped porous carbon with secondary heteroatoms. *Appl. Catal. B: Environ.* **2020**, *266*, 118633.

This is an open access article under the terms of the Creative Commons Attribution 4.0 International License (CC BY 4.0, https://creativecommons.org/licenses/by/4.0/).

© The Author(s) 2026. Published by Tsinghua University Press.